

# Strong control of effective radiative forcing by the spatial pattern of absorbing aerosol

Andrew Williams (✉ [andrew.williams@physics.ox.ac.uk](mailto:andrew.williams@physics.ox.ac.uk))

University of Oxford <https://orcid.org/0000-0002-5457-5075>

Philip Stier

University of Oxford <https://orcid.org/0000-0002-1191-0128>

Guy Dagan

University of Oxford <https://orcid.org/0000-0002-8391-6334>

Duncan Watson-Parris

University of Oxford <https://orcid.org/0000-0002-5312-4950>

---

## Article

**Keywords:** anthropogenic aerosol, climate change, effective radiative forcing, atmospheric dynamics

**Posted Date:** December 1st, 2021

**DOI:** <https://doi.org/10.21203/rs.3.rs-1015938/v1>

**License:** © ⓘ This work is licensed under a Creative Commons Attribution 4.0 International License.

[Read Full License](#)

---

**Version of Record:** A version of this preprint was published at Nature Climate Change on July 21st, 2022.

See the published version at <https://doi.org/10.1038/s41558-022-01415-4>.

# Strong control of effective radiative forcing by the spatial pattern of absorbing aerosol

Andrew Williams<sup>1\*</sup>, Philip Stier<sup>1</sup>, Guy Dagan<sup>1,a</sup>, Duncan Watson-Parris<sup>1</sup>

<sup>1</sup>Atmospheric, Oceanic and Planetary Physics, Department of Physics, University of Oxford, UK

<sup>a</sup> Now at: The Hebrew University of Jerusalem, Israel

\*Correspondence to: [andrew.williams@physics.ox.ac.uk](mailto:andrew.williams@physics.ox.ac.uk)

## **Abstract**

Over the coming decades it is expected that the spatial pattern of anthropogenic aerosol will change dramatically and that the global composition of aerosols will become relatively more absorbing. However, despite this the climatic impact of the evolving spatial pattern of absorbing aerosol has received relatively little attention, in particular the impact of this pattern on global-mean effective radiative forcing. Here we use novel climate model experiments to show that the effective radiative forcing from absorbing aerosol varies strongly depending on their location, driven by rapid adjustments of clouds and circulation. Our experiments generate positive effective radiative forcing in response to aerosol absorption throughout the midlatitudes and most of the tropical regions and a strong ‘hot spot’ of negative effective radiative forcing in response to aerosol absorption over the Western tropical Pacific. We show that these diverse responses can be robustly attributed to changes in atmospheric dynamics and highlight the importance of this previously unknown ‘aerosol pattern effect’ for transient forcing from regional biomass-burning aerosol.

## **Main**

Anthropogenic aerosol plays a significant role in determining the influence of human activities on climate<sup>1-3</sup>. Due to their short lifetimes, the spatial pattern of anthropogenic aerosol is highly heterogenous, and this has been shown to impact on climate through changes in atmospheric circulation<sup>4,5</sup>, tropical precipitation<sup>5-8</sup> and sea-surface temperature (SST) patterns<sup>6,9,10</sup>, with implications for the transient climate response<sup>11</sup>.

5 Over the coming decades, emissions of anthropogenic aerosol are expected to change dramatically both in their  
6 spatial pattern and composition<sup>3</sup>, particularly over South-East Asia and Central Africa<sup>2,3</sup>. These trends are further  
7 complicated by the fact that policy measures often target sources of scattering and absorbing aerosols differently,  
8 such that even with no net change in aerosol optical depth (AOD), there could be climatic impacts from changes  
9 in aerosol composition<sup>12</sup>. Such a trend is already being seen globally; while the global anthropogenic AOD has  
0 been roughly constant since the 1980s, the contribution from aerosol absorption has almost doubled over this  
1 period<sup>3,13</sup>. In the future, particularly under weak air-quality policies, these trends towards a more absorbing aerosol  
2 distribution are likely to continue<sup>2</sup>.

3  
4 Given these observations, a key question arises: how does the evolving spatial pattern of anthropogenic aerosol  
5 (particularly absorbing aerosols, hereafter ‘AAs’) impact on climate? Crucially, how does the effective radiative  
6 forcing (ERF) - defined as the net change in radiative fluxes at the top-of-atmosphere in a fixed-SST experiment  
7 following a change in forcing agent, allowing for rapid adjustments<sup>14</sup> - respond to this changing pattern of AAs?  
8 A robust answer to this question would have substantial ramifications because the spatial pattern of aerosol is not  
9 considered either in the simple climate models<sup>15,16</sup> or integrated assessment models<sup>17</sup> which form an essential part  
0 the IPCC process<sup>18</sup>.

1  
2 Without accounting for the evolving spatial pattern of aerosol, it is implicitly assumed that there is a one-to-one  
3 mapping between global AOD (or emissions) and ERF for a given single-scattering albedo (i.e., a constant  
4 ‘forcing efficiency’). However, the existence of such a one-to-one mapping is not obvious given the complex  
5 regional interactions between aerosols, clouds and the large-scale circulation. This is particularly true of AAs,  
6 with a single-scattering albedo less than 1, which absorb incoming solar radiation and locally heat the  
7 atmosphere<sup>19</sup>. In the tropics, where clouds and circulation are inextricably linked through phase-changes, radiative  
8 transfer and SST patterns<sup>20</sup>, this AA-induced diabatic heating causes significant changes which can either amplify  
9 or reduce the impact of the initial perturbation<sup>21–25</sup>.

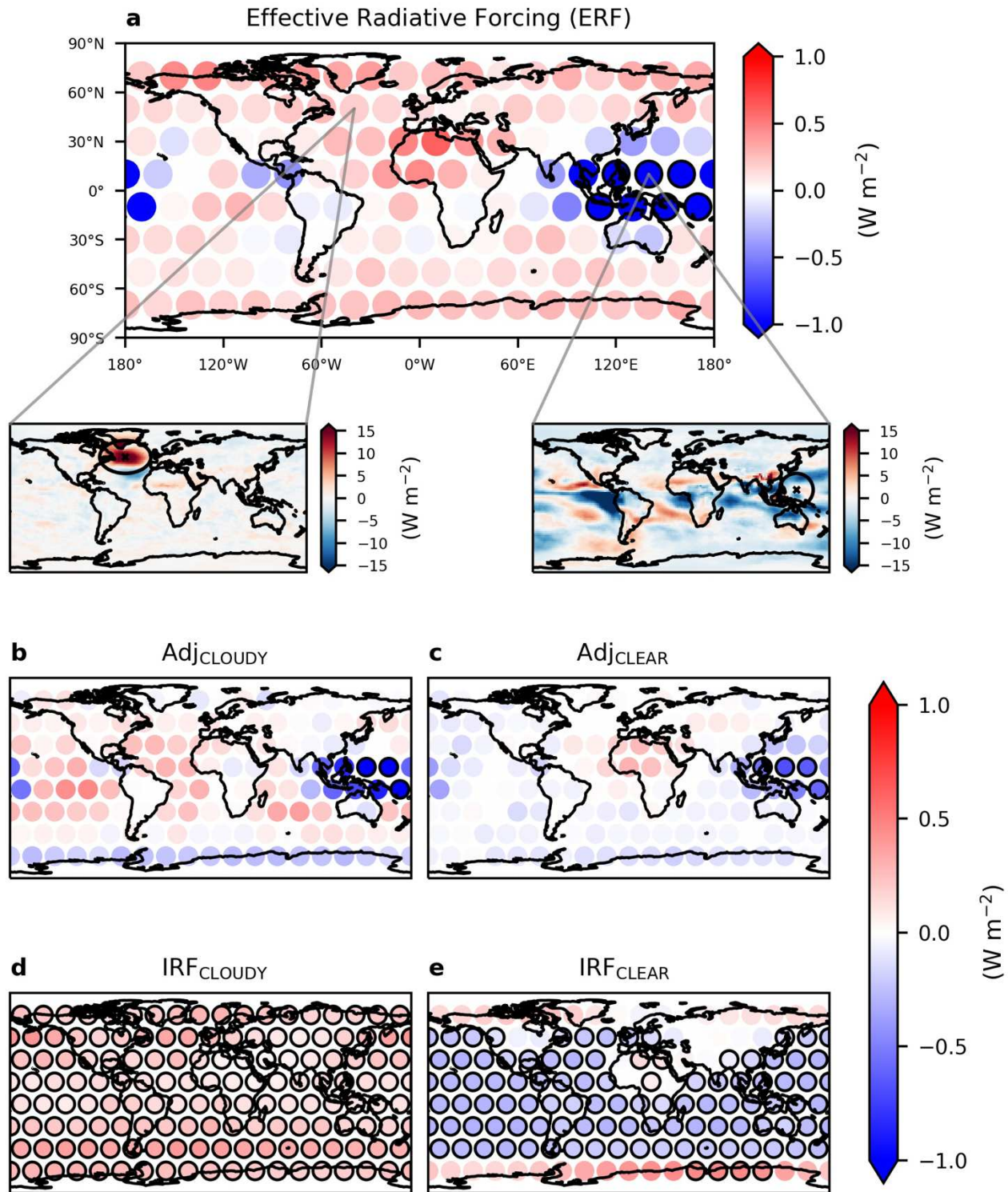
1 Previous studies of the spatial pattern of aerosol have focused either on climatological aerosol distributions<sup>26,27</sup>,  
2 perturbations to aerosol concentrations or solar forcing in different latitude bands<sup>5,28–30</sup> or emissions changes in a  
3 small number of geopolitical regions<sup>31–33</sup>. However, these studies have several limitations. Firstly, the distribution  
4 of aerosol in the tropics is often dominated by large, transient biomass-burning events, which are not well-  
5 represented in climatologies<sup>34–36</sup> and have a distinct longitudinal structure. Secondly, the use of local changes in  
6 solar forcing is limiting, as aerosol emissions can trigger non-local changes in ERF. Additionally, the translation  
7 from emissions to concentrations is highly uncertain<sup>37</sup> and depends strongly on the lifetime of the aerosols<sup>25</sup>.  
8 Finally, the use of different models with different setups, each often focussing on a small number of case study  
9 regions, makes it difficult to disentangle the impact of aerosols in different locations. This is important for policy  
0 as future aerosol distributions may differ significantly from what has been observed over the historical period<sup>3</sup>.

1  
2 To tackle this, here we present a large ensemble of simulations with a state-of-the-art, atmosphere-only global  
3 climate model (GCM) forced with idealized AOD perturbations placed systematically across the globe. This  
4 approach allows us to explore the sensitivity of ERF to localized aerosol absorption without being biased towards  
5 specific regions. Our results demonstrate a strong dependence of global-mean ERF on the spatial pattern of AAs,  
6 which is controlled mainly by the dynamical response of atmospheric circulation and clouds to aerosol heating in  
7 different locations. Finally, we highlight the significance of our results for large, transient ERF from Indonesian  
8 peatland wildfires, which generate AA perturbations that sit directly on a ‘hot spot’ of ERF sensitivity in our  
9 experiments.

### 1 **Dependence of ERF on the location of absorbing aerosol**

2 Figure 1a illustrates the global-mean ERF in response to the 144 separate aerosol plume experiments conducted.  
3 The AOD perturbations are prescribed using two-dimensional Gaussian distributions in the horizontal, with an  
4 amplitude of 1 at their centre (Methods). The global-mean AOD perturbation is the same in each experiment  
5 and only the location is varied (Supplementary Fig. 1). The single-scattering albedo at 550nm is set to 0.8 in  
6 each experiment, corresponding to strongly absorbing aerosol<sup>19</sup>. The variations in ERF in Fig. 1a illustrate that

7 the ERF from a certain global-mean AA perturbation depends strongly on how the AAs are spatially distributed.  
8 For example, when the AAs are concentrated in the extratropics, the ERF is generally positive, whereas when  
9 the AA is located over the Western tropical Pacific there is a strong negative ERF in the global-mean. The two  
0 insets below Fig. 1a show that the spatial pattern of the ERF also varies markedly depending on the plume  
1 location, with an extratropical plume generating a positive, local increase in ERF, whereas the plume over the  
2 Western tropical Pacific generates a global-scale ERF perturbation, with large regions of positive and negative  
3 response.



4

5 *Figure 1. a* ICON GCM simulated global- and time-mean effective radiative forcing (ERF) calculated as the net TOA flux difference  
 6 *between simulations with the AA perturbation and the control experiment. Each filled circle denotes the global-mean results from the*  
 7 *experiment with the idealized AA plume centered on that location, and the size of the plumes is illustrated by Supplementary Fig. 1.*  
 8 *Enclosing black circles are present where the resultant radiative forcing is statistically significant at the 1-sigma level. Two insets are*  
 9 *also present showing the spatial pattern of ERF changes for two illustrative plume experiments. In each of these subplots the center of*  
 0 *the AA perturbation in that experiment is marked with a marker and its size illustrated by an ellipse which contains 95% of the total*  
 1 *AOD perturbation in that experiment. Ellipses are used in the insets to represent the distortion introduced by the map projection. b-e*  
 2 *Decomposition of the total ERF into contributions from fast-adjustments (Adj) and instantaneous radiative forcing (IRF) in clear- and*  
 3 *cloudy- sky.*

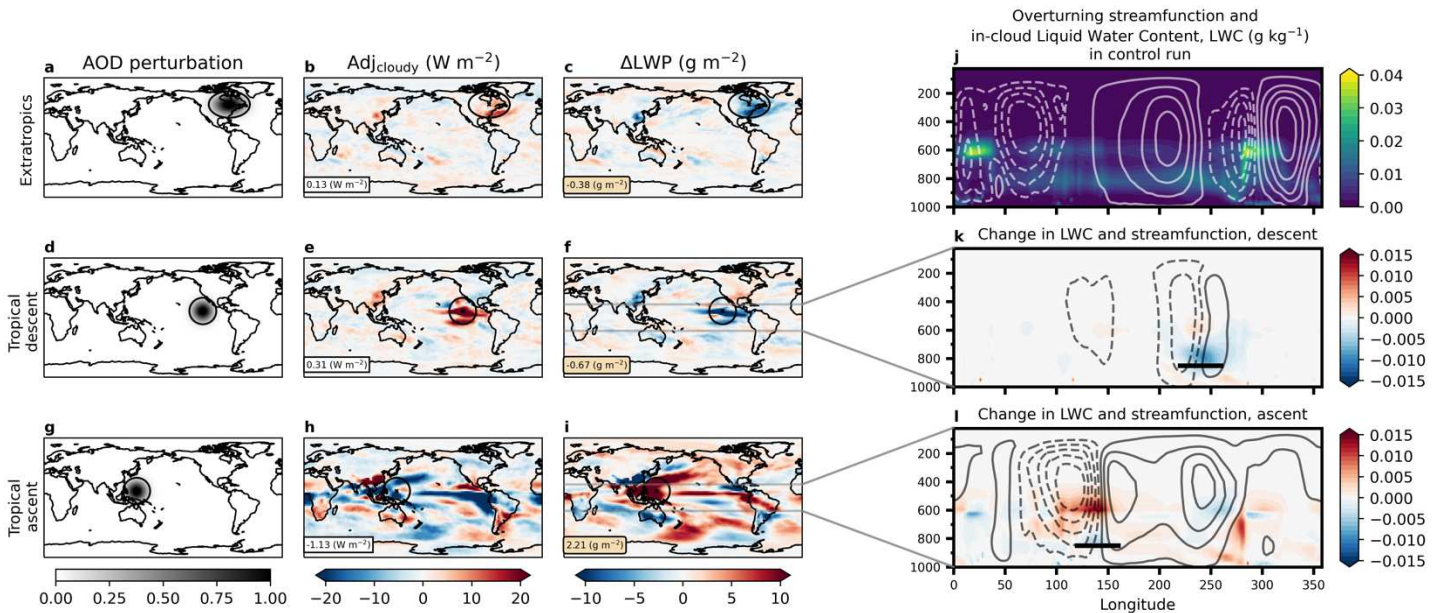
4  
5 Next, we decompose the ERF into contributions from instantaneous radiative forcing (IRF) and rapid  
6 adjustments (Adj) and analyse these in clear- and cloudy-sky. This allows us to disentangle the direct, radiative  
7 effect of the AAs (the instantaneous forcing) from their influence on circulation and cloudiness (the  
8 adjustments). Figure 1d,e illustrates how for most of the plumes, the contribution from IRF is a balance between  
9 the changes in clear- and cloudy-sky, resulting in an overall small contribution from IRF in most cases. This is  
0 consistent with previous work<sup>38</sup> which has demonstrated that the IRF of AAs becomes positive when the  
1 effective albedo of the underlying surface rises above a critical value. Thus, the cloudy-sky IRF is generally  
2 positive because low clouds serve as a high-albedo surface, whereas the clear-sky IRF is negative for most  
3 perturbation sites except for over high-albedo surfaces such as the Sahara or the high-latitudes.

4  
5 Variations in global-mean ERF in response to AAs is mainly caused by variations in the global-mean  
6 adjustments, as shown in Fig. 1b and c. The rapid adjustments in clear-sky are well-explained by changes in  
7 clear-sky outgoing longwave radiation arising from global-mean temperature changes (Supplemental Fig. 2)  
8 and contribute negatively to the total ERF for most locations except the Sahara and the Western tropical Pacific,  
9 where they amplify the cloudy-sky contribution. Overall, the cloudy-sky rapid adjustments (Fig. 1b) account for  
0 over 63% of the total variation in ERF in response to AAs in different locations and are the key determinant of  
1 the ‘hot spot’ of ERF in the Western tropical Pacific. Hence, we mainly focus our attention on the cloudy-sky  
2 adjustments.

#### 4 **Circulation changes control the location-dependence of ERF**

5 Cloudy-sky adjustments are strongly anti-correlated with global-mean liquid water path (LWP) changes across  
6 all our experiments (Supplementary Fig. 3) because higher LWP is associated with optically thicker clouds which  
7 reflect more incoming solar radiation. But why do AAs in some locations cause such an increase in LWP while  
8 others cause a decrease? Shortwave absorption from AAs introduces a positive temperature tendency to the local  
9 atmospheric column, and in the absence of terms which balance this tendency the temperature in this region would

0 increase without bound. However, in the extratropics (Fig. 2a), temperature anomalies generate a downstream  
 1 low-pressure system due to potential vorticity conservation<sup>39</sup> which draws down cold air from higher latitudes  
 2 (Supplementary Fig. 4). This cold-air advection in response to AAs in the extratropics is a negative feedback  
 3 which balances the temperature tendency from the AAs, generating a finite, localized temperature increase. Other  
 4 local processes such as radiative cooling or precipitation feedbacks also contribute to balancing the temperature  
 5 tendency from the AAs (Supplementary Fig. 7). This temperature increase causes a decrease in relative humidity,  
 6 which inhibits cloud formation and decreases LWP in the region of the AA perturbation (Fig. 2c). This mechanism  
 7 explains the broad pattern of positive cloudy-sky adjustments (Fig. 1b) and negative LWP changes  
 8 (Supplementary Fig. 3) throughout the extratropics.

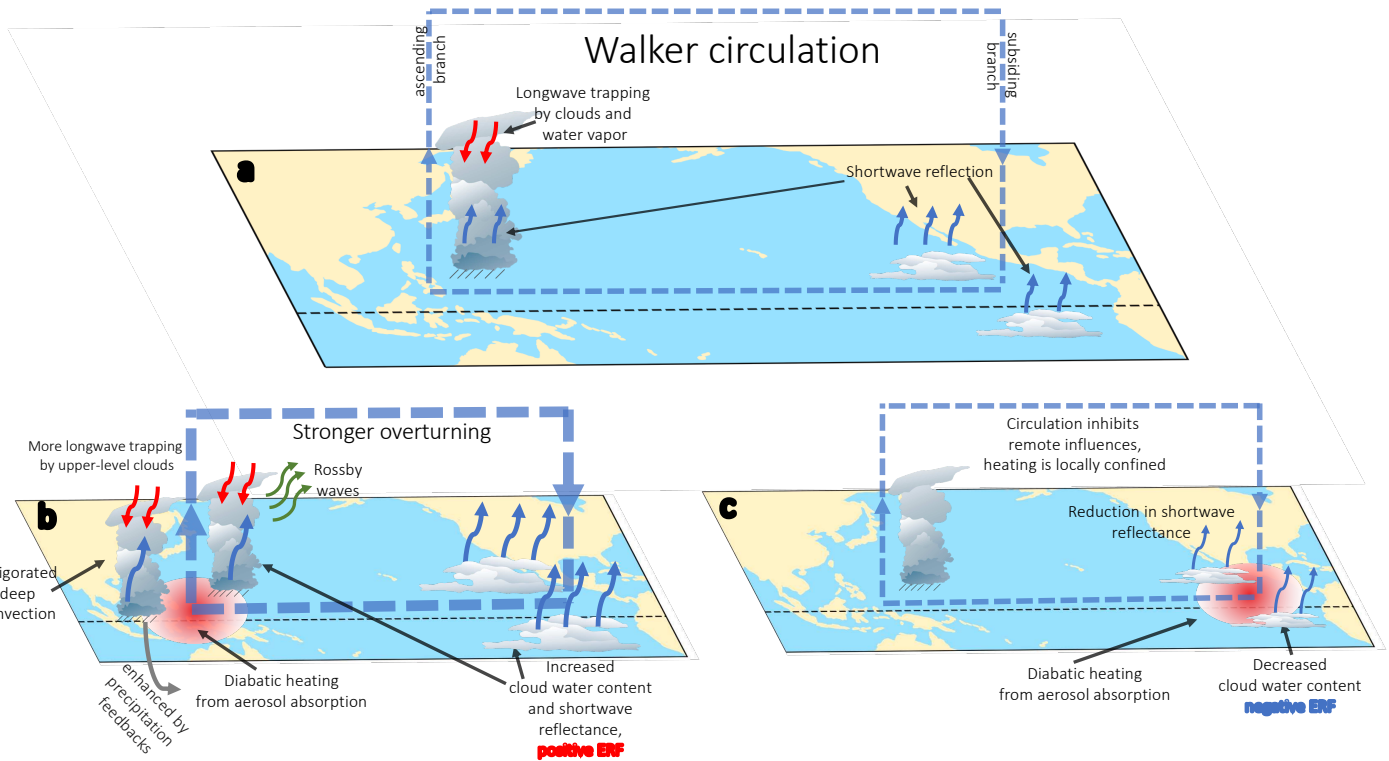


9  
 0 *Figure 2. Time-mean AOD perturbation, cloudy-sky adjustments ( $Adj_{cloudy}$ ) and in-cloud liquid-water path (LWP) changes for*  
 1 *idealized AA perturbations in; the extratropics (a-c), a tropical descent region (d-f) and a tropical ascent region (g-i). Black ellipses*  
 2 *illustrate the horizontal size of the perturbation in each experiment, and the global-mean values for (b, c, e, f, h, i) are shown in*  
 3 *boxes. Panel j shows a pressure-longitude cross-section of the in-cloud liquid water content (colours) and zonal mass stream-function*  
 4 *(contours) in the control simulation, averaged between 20° either side of the equator (the horizontal grey lines in f, i). Panels k and l*  
 5 *show the changes in these quantities in response to AA perturbations in the East and West Pacific, respectively. The contour interval*  
 6 *in panels (j-l) is  $4 \times 10^{10} kg s^{-1}$  and solid contours indicate clockwise overturning. In panels k and l, horizontal black lines illustrate the*  
 7 *horizontal extent of the AOD perturbation, at a height corresponding roughly to the maximum of the plume AOD profile (see*  
 8 *Methods).*

0 A similar, localized decrease in LWP occurs when the AAs are in a region of tropical descent (Fig. 2d-f), however  
 1 the mechanism is quite distinct. In the tropics, as the Coriolis force is weak, the diabatic heating from AAs is  
 2 balanced mostly by vertical motion<sup>40</sup>, generating a thermally-direct overturning circulation<sup>40</sup>. However, when the

3 AA perturbation is in a region of large-scale descent - in this case, the descending branch of the Pacific Walker  
 4 cell<sup>41</sup> (Fig. 2j) - the anomalous overturning from the diabatic heating interacts destructively with the existing  
 5 large-scale descent and becomes confined to local scales, causing a decrease in low-level liquid water content  
 6 (Fig. 2k).

7  
 8 Conversely, when the AA perturbation is placed in a region of large-scale tropical ascent (Fig. 2g), the  
 9 anomalous vertical motion generated by the diabatic heating projects onto this existing mode of variability,  
 0 amplifying the Walker circulation and increasing the upper-level divergence. This pattern of low-level  
 1 convergence and upper-level divergence excites equatorial waves which generate large, positive LWC  
 2 anomalies throughout the tropics (Fig. 2i, l), and planetary-scale Rossby waves which communicate the  
 3 perturbation to the midlatitudes<sup>39</sup> (Fig. 2i). A schematic representation of our results is given in Fig. 3.



4  
 5 *Figure 3: Schematic representation of the processes governing location-dependence of the radiative forcing from absorbing aerosols*  
 6 *in the tropics. Panel a illustrates the tropical overturning circulation in the control simulation. Panel b shows how aerosol absorption*  
 7 *in the ascending branch of the overturning circulation leads to a strong increase in shortwave reflectance throughout the tropics.*  
 8 *Panel c on the other hand shows that when aerosol absorption is put in the subsiding branch of an overturning cell, the subsidence*  
 9 *confines the heating anomaly to local scales, inhibiting cloud formation and causing a local decrease in shortwave reflectance.*

1 To distill the key physical mechanisms, we conducted another set of AA perturbation experiments in a  
 2 simplified aquaplanet model forced by an SST-dipole along the equator (a ‘mock-Walker’ circulation,  
 3 Methods). This generates an overturning circulation with similar characteristics to the Walker circulation in our  
 4 control experiment (Supplementary Fig. 5). Again, we find that when the AAs are located over the warm pool  
 5 region, there is a strengthening of the circulation and a large increase in LWP which drives a shortwave cloudy-  
 6 sky adjustment, although this is offset somewhat by increases in upper-level ice, which contributes negatively to  
 7 the cloudy-sky adjustments. Similar increases in upper-level cloud ice are found in our main experiments,  
 8 though to a lesser extent (Supplementary Fig. 6).

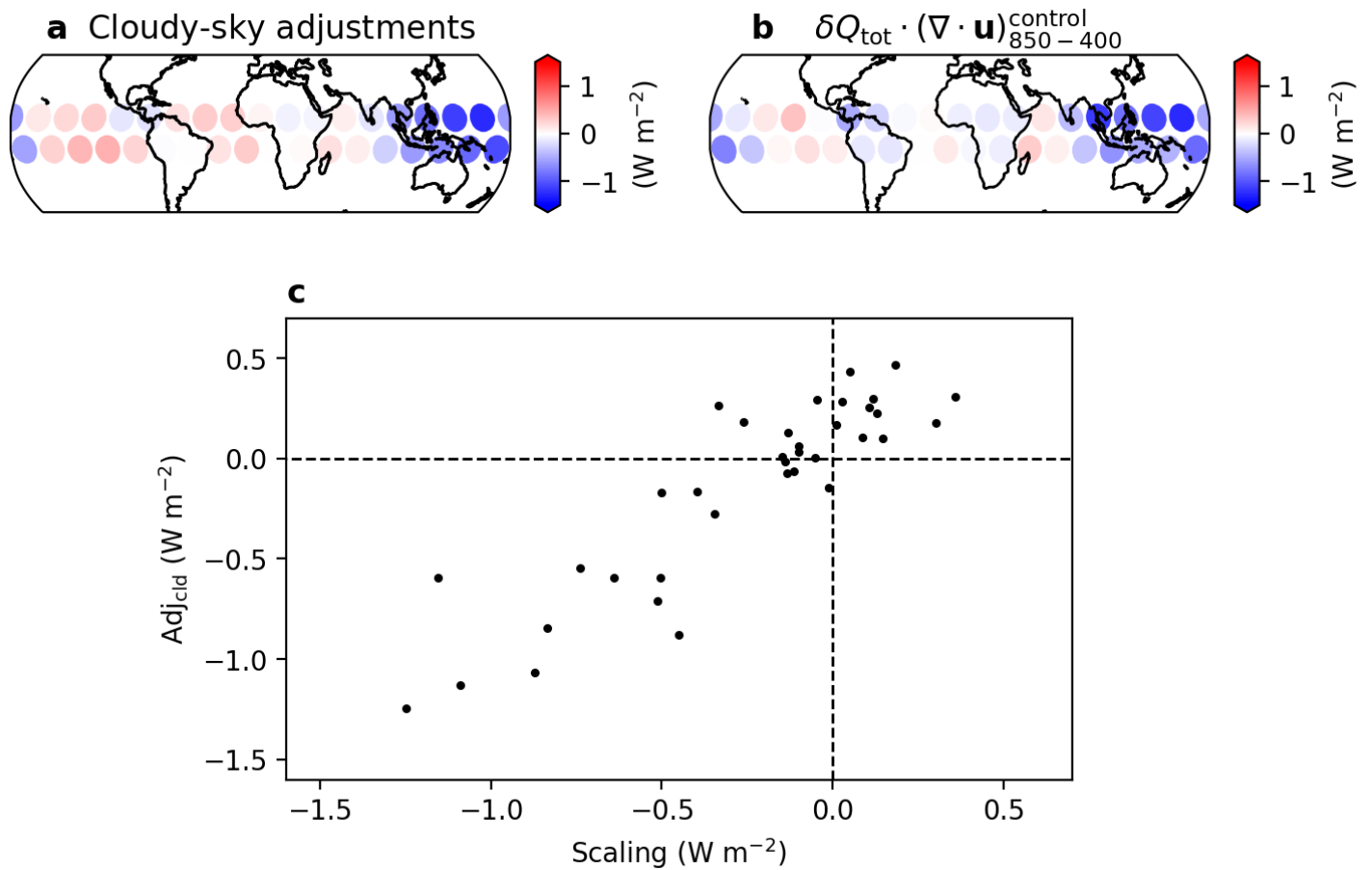
9  
 0 Over land, there is greater convective inhibition due to lower boundary-layer relative humidity<sup>42</sup>, which inhibits  
 1 the upward motion associated with diabatic heating in the tropics. This helps explain why similarly large ERFs  
 2 are not seen in response to AAs over South America and the African monsoon regions (which are also associated  
 3 with large-scale ascent). Additionally, AAs cause a large surface cooling in our experiments when located over  
 4 land<sup>22</sup>, which drives a reduction in the surface sensible heat flux and a reduction in the diabatic heating  
 5 perturbation for AAs over land (Supplementary Fig. 7c), explaining the land-ocean contrast in Figure 1b.  
 6 Adjustments of clouds and precipitation can also impact the diabatic heating perturbation through changes in  
 7 latent heat release or by reductions in outgoing longwave radiation (Supplementary Fig. 7b,f).

8  
 9 To assess how well this explanation captures the simulated variations in cloudy-sky adjustments (and thus,  
 0 ERF) across the tropics, we quantify it with a simple scaling,

$$1 \quad \text{Adj}_{\text{cld}} \sim \delta Q_{\text{tot}} \cdot (\nabla \cdot \mathbf{u})_{850-400}^{\text{control}}, \quad (1)$$

2  
 3  
 4 where  $\delta Q_{\text{tot}}$  is the total diabatic heating from the plume (including latent heating) and  $(\nabla \cdot \mathbf{u})_{850-400}^{\text{control}}$  is the  
 5 difference between the horizontal divergence at 850hPa and 400hPa in the control run. Both quantities are  
 6  
 7  
 8  
 9

6 averaged within a fixed radius of the center of the AOD perturbation in that experiment. Similar results are  
 7 obtained if we replace  $(\nabla \cdot \mathbf{u})_{850-400}^{\text{control}}$  with the local vertical velocity at 850hPa (Supplementary Fig. 8).  
 8  
 9 Figure 4 shows that Eq. (1) captures the variation in simulated cloudy-sky adjustments in response to AAs  
 0 across the tropics and demonstrates that this can be understood quantitatively in terms of simple tropical  
 1 dynamics, as illustrated in Figure 3. Notably, the scaling also successfully predicts the ‘hot spot’ of negative  
 2 ERF over the Western tropical Pacific.



3  
 4 *Figure 4. Map of the global-mean, cloudy-sky rapid adjustments from tropical AA experiments (a) and the corresponding estimate when using a simple, circulation-based*  
 5 *scaling which relates the total diabatic heating from the AAs and the local, vertical shear of the horizontal divergence in the control run to the cloudy-sky adjustments,*  
 6 *(b). Panel c shows a scatter plot of the results in panels a and b. In panels b and c, the scaling was evaluated in S.I. units (W m<sup>-2</sup> s<sup>-1</sup>) and then, for plotting purposes, each*  
 7 *scaling estimate was multiplied by the same dimensional constant such that the results match the magnitude of the cloudy-sky adjustments in panels a, this does not affect*  
 8 *the correlation.*

### 0 Implications for Indonesian biomass-burning events

1 This strong ‘hot spot’ of ERF over the Western tropical Pacific region raises the question: could this have real  
 2 world implications? One potential candidate is Indonesian wildfire events. Wildfires have been recorded in this  
 10

region since the late-Pleistocene<sup>43</sup>, however the worst known fires have occurred since the 1980s due to changes in land-use and population density<sup>34</sup>. Large peat deposits make Indonesian wildfires uniquely impactful since peat is highly combustible and difficult to extinguish, and peat fires have repeatedly led to high AOD, ‘haze’ events<sup>36</sup>. Figure 5a shows a time-series of ground-based observations of mid-visible AOD from five Aerosol Robotic Network (AERONET) sites located in Indonesia. There is significant biomass-burning in the dry seasons in most years, particularly 2015 (associated with a strong El Nino) and 2019 (without an El Nino, but with a positive Indian Ocean Dipole).

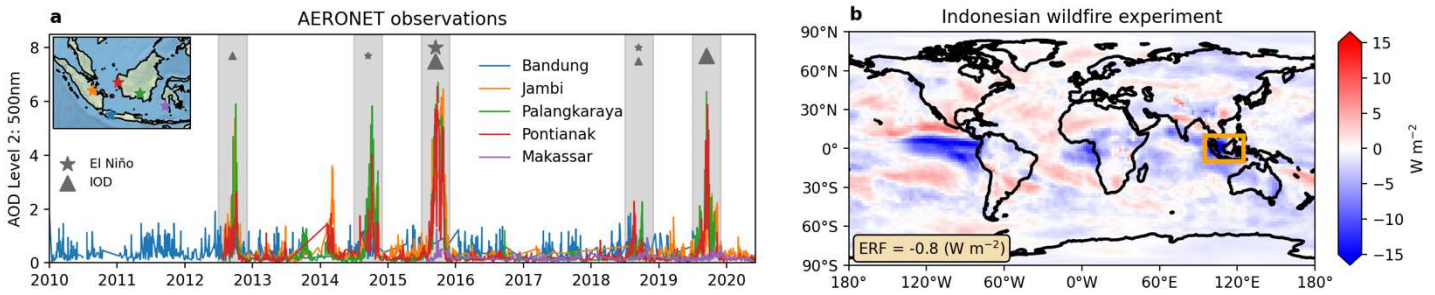


Figure 5: **a** Timeseries of aerosol optical depth at 500nm from five AERONET sites in Indonesia. Grey shading denotes dry seasons with significant biomass-burning. Years with an El Nino event are shown with a star and years with an IOD event are shown with a triangle, the size of the marker illustrates the magnitude of the event. **b** Map of the time-mean ERF from our ‘Climatology x16’ experiment (see Methods). The orange box shows the region corresponding to the inset in panel **a** and illustrates the approximate area of the AOD perturbation in this experiment (Supplementary Fig. 6).

To investigate whether these events could generate large ERF as suggested by our idealized experiments, we conduct experiments using a realistic AOD climatology of Indonesian biomass-burning (Methods), with a seasonal cycle which peaks in the dry season (Supplementary Fig. 9). We perform five experiments in which we successively double the climatological Indonesian plume AOD until the peak dry-season AOD is comparable to the 2015/2016 observations<sup>36</sup>, corresponding to 16 times the climatological AOD (Methods). Figure 5b shows the ERF from this experiment and demonstrates that despite the introduction of a seasonal cycle and use of a more realistic AOD distribution, the spatial pattern is remarkably like our idealized simulations over the ‘hot spot’ (e.g., Fig. 2h).

The global-mean ERF scales linearly with the AOD burden in each of the experiments (Supplementary Fig. 10), which provides evidence that the reason large ERF has not been noted in previous studies which use

7 climatological AOD distributions<sup>29</sup> or emissions from a single-year<sup>44</sup> is not because we have misunderstood the  
8 physics, but rather because these large biomass-burning events are under-represented in climatological  
9 distributions and have strong inter-annual variability.

1 Tropical SST variability such as ENSO also plays a role by modulating the pattern of tropical overturning and  
2 generating anomalous subsidence over this region, which would inhibit the remote influence on LWP and ERF  
3 we see in our experiments (Figure 3). This helps to explain why previous studies on the ERF of the 1997  
4 Indonesian wildfire<sup>45</sup> (also associated with a strong El Nino) have found a positive ERF, localized to small scales.  
5 Our proposed mechanism predicts such a response (Fig. 3).

## 7 **Discussion**

8 In summary, our knowledge of how the climatic impact of aerosol depends on its spatial pattern is lacking as  
9 previous studies have often focused only on a small number of regions. To address this, we have conducted a  
0 series of experiments with a state-of-the-art climate model in which identical AOD perturbations we placed across  
1 the globe. We have shown, contrary to the assumption commonly made in previous studies, that the ERF of  
2 absorbing aerosol depends strongly on its spatial pattern, with even the sign of the forcing varying markedly  
3 between different perturbation sites. In the extratropics, we find that meridional advection of high latitude air  
4 ‘confines’ the heating anomaly from the AAs to local scales and drives a positive ERF through reductions in LWP  
5 local to the plume. On the other hand, in the tropics the ERF is determined by interactions between the diabatic  
6 heating and the structure of the tropical overturning circulation. In regions of large-scale descent, the diabatic  
7 heating anomaly is confined to local scales, generating a similar response to the extratropical case. However, in  
8 regions of large-scale ascent the AAs excite significant wave activity which generates positive LWP anomalies  
9 across the globe and a strong, negative ERF.

1 Of particular interest is the ‘hot spot’ of negative ERF we identify in response to AAs over the Western tropical  
2 Pacific, which suggests there could be large, transient ERF from seasonal biomass-burning over this region. We  
3 explored this question using a realistic climatology of Indonesian biomass-burning, constrained by AERONET  
4 observations during the 2015/2016 wildfire event, and showed that significant ERF of  $\sim O(-1\text{Wm}^{-2})$  is possible  
5 via our proposed mechanism. Our results demonstrate that Indonesian biomass-burning could represent a  
6 significant source of negative ERF on interannual timescales, particularly during non-ENSO years<sup>46</sup>.

7  
8 Although it is known that non-local circulation adjustments can influence ERF<sup>47</sup>, previous work has questioned  
9 their importance compared to local thermodynamic changes<sup>44</sup>. For example, Johnson et al., (2019) showed that  
0 suppressing circulation changes with nudging did not impact their estimates of global-mean ERF. However, their  
1 experiment used emissions from a single year (2014) which did not have significant biomass burning over the  
2 Western tropical Pacific. In contrast, for the case of AAs, our results demonstrate that non-local circulation  
3 adjustments can play a first-order role in determining the ERF, even on global-mean scales. This suggests that,  
4 while nudged experiments can be useful for diagnosing ERFs dominated by scattering aerosol, caution is needed  
5 when using nudged experiments to determine the ERF from AAs.

6  
7 Although our analysis does not explore inter-model differences, given the robustness of the response across a  
8 hierarchy of model configurations and its interpretability in terms of robust atmospheric dynamics, it is unlikely  
9 we would find qualitatively different sensitivities in a different GCM. However, given the difficulty in correctly  
0 representing convection in models, future work should leverage the emerging power of global cloud-resolving  
1 models<sup>48</sup> to build confidence in the physical processes driving this pattern of ‘forcing efficiency’. Furthermore,  
2 our experiments focus on the ERF from aerosol-radiation interactions and neglect the ‘indirect’ impacts of  
3 aerosol on cloud microphysical processes. However, given the uncertainty surrounding the microphysical  
4 interactions between clouds and absorbing aerosol<sup>27,49</sup> we consider this a reasonable limitation of our study,

5 especially because that the uncertainty in ERF from aerosol-radiation interactions is comparable to that from  
6 aerosol-cloud interactions<sup>47</sup>.

## 9 **Methods**

### 0 **Idealized simulations**

1 An ensemble of 145 fixed-SST simulations were conducted using the ICON (ICOsahedral Non-hydrostatic) general circulation  
2 model<sup>25</sup>/10/2021 12:07:00. This configuration of the ICON model uses the ECHAM6 physics packages<sup>50</sup>, including a bulk mass-flux  
3 convection scheme<sup>51,52</sup> and cloud cover calculated locally in each grid box using a relative humidity scheme<sup>53</sup>. Other parametrization  
4 schemes used are the Lohmann and Roeckner cloud microphysics scheme<sup>54</sup> and the PSrad radiative transfer scheme<sup>55</sup>, which  
5 implements the gas radiative transfer and solvers from the widely used Rapid Radiation Transfer Model<sup>56</sup>. We have extended the  
6 model so that the total aerosol radiative effect is calculated at every radiation time-step by performing a double-call to the radiation  
7 scheme with and without the aerosol perturbation and then subtracting the results, the instantaneous radiative forcing (IRF) is then  
8 calculated by differencing the total aerosol radiative effect between a perturbed run and the control.

9 The simulations were run on a triangular grid (R02B04 specification) with a 223km edge length, corresponding to an average grid  
0 spacing of approximately 157.8km on a Cartesian grid. The model uses a terrain-following vertical sigma-height grid<sup>57</sup> with 47 levels  
1 between the surface and the model top at 83km. Each simulation, including the control run, is integrated for 20 years with timesteps of  
2 15 minutes and 90 minutes for the dynamics and radiation, respectively, after which the first year is discarded as spin-up and analysis  
3 is conducted over the remaining 19 years. The simulation length was chosen as a trade-off between computational constraints and the  
4 requirement that our runs are long enough to give robust results in the face of internal variability. In terms of radiative forcing, Forster  
5 et al. (2016) demonstrated that a five-year run is sufficient to obtain robust statistics for the effective radiative forcing relative to a  
6 control run, and a single year is sufficient for obtaining values of the instantaneous radiative forcing<sup>58</sup>.

7 As a further attempt to reduce variability due to trends in atmospheric composition, each simulation is run with greenhouse gases and  
8 ozone fixed at their 1979 levels. Additionally, the simulations are also forced by climatological monthly sea-surface temperatures  
9 (SSTs) and sea-ice concentrations derived from Atmospheric Model Intercomparison Project<sup>59</sup> boundary conditions over 1979-2016  
0 (AMIP), eliminating SST-driven variability such as the El-Nino Southern Oscillation (ENSO) which could otherwise bias the results.  
1 Supplementary Fig. 1 c and d illustrates the annual-mean SST field used to force the model, demonstrating neutral ENSO conditions  
2 with a warm pool in the Western Pacific and a cold pool in the Eastern Pacific.

3           Aside from the control run, the only difference between the remaining 144 simulations is the inclusion of an idealized plume  
4 of absorbing aerosol at 144 different geographical locations (Supplementary Fig. 1a), parametrized using the Max Planck Institute  
5 Aerosol Climatology version 2, Simple Plume (MACv2-SP) model<sup>60</sup>. The plume’s horizontal structure is specified to be a 2-  
6 dimensional Gaussian function with a standard deviation of 10° degrees. The vertical distribution of aerosol is based on the kernel of  
7 Euler's  $\beta$ -function (see details in Stevens et al., 2017), with most of the aerosol concentrated in the lower 3km of the atmosphere and a  
8 peak at ~1km (Supplementary Fig. 1b). We note that differences in the vertical plume profile may cause different responses of the  
9 climate system and general circulation<sup>24,61,62</sup>, however Kinne et al. (2013) found that a vertical distribution like ours is broadly-  
0 representative of the vertical structure of fine-mode AOD<sup>63</sup>. Both the horizontal and vertical structure of the plume are constant in time  
1 and the shape of the plume is not influenced by the local meteorology.

2           In each of the aerosol perturbation experiments the plume is prescribed with a total column AOD=1 and a single-scattering  
3 albedo (SSA) of 0.8, both defined at a wavelength of 550nm. This corresponds to a strongly absorbing plume of aerosol, generating a  
4 large diabatic heating perturbation in the lower atmosphere, even while generating cooling at the surface. Furthermore, to isolate the  
5 role of the radiative impact of the plume we do not include the microphysical effects of the aerosol plume which are also described in  
6 Stevens et al. (2017), so the radiative forcing we calculate is the  $ERF_{ARI}$  in the framework of AR5.

7           The location of the 144 idealized aerosol plumes was chosen to provide broad coverage over the entire globe, while also  
8 ensuring that there are several plumes in semi-realistic locations. For example, our setup includes plumes over Europe, North  
9 America, South America, Australia, China, India, Central Africa, and the Maritime Continent alongside far less realistic plumes of  
0 absorbing aerosol over the remote oceans and polar regions. We choose to take this approach for two reasons: firstly, although aerosol  
1 perturbations are highly localized over their source region, it is possible for them to be advected long distances by the large-scale  
2 circulation. Secondly, although many of these plumes are less realistic, they allow us to sample many different surface properties and  
3 local and large-scale meteorological conditions, which aids us in building a physical picture of what sets the response.

#### 4 **Calculation of ERF and fast adjustments**

5 We calculate the effective radiative forcing (ERF) as the difference between the net top-of-atmosphere (TOA) radiative fluxes  
6 between a perturbation experiment and the control (after discarding the first year as spin-up, and taking averages over the subsequent  
7 19 years), following the suggestion of Forster et al. (2016). All experiments are conducted with fixed-SSTs and sea-ice concentrations.  
8 We then use the instantaneous radiative forcing (IRF), diagnosed as the difference between aerosol radiative effect in the perturbed  
9 and control experiments, to calculate the contributions from fast-adjustments in clear- and cloudy-sky as:

$$Adj_{clear} = ERF_{clear} - IRF_{clear}$$

$$\text{Adj}_{\text{cloudy}} = \text{ERF}_{\text{cloudy}} - \text{IRF}_{\text{cloudy}}$$

Where  $\text{ERF}_{\text{clear}}$  and  $\text{ERF}_{\text{cloudy}}$  are defined the same as the ERF but only using TOA fluxes in clear- and cloudy- sky, respectively.

### Clear-sky rapid adjustments

To understand the variations in clear-sky rapid adjustments, we note that, globally, the outgoing longwave radiation (OLR) can be written as:

$$\text{OLR} = \epsilon \sigma T^4 \quad (1)$$

Where  $\sigma T^4$  is the surface blackbody emission, and  $\epsilon$  is an ‘effective emissivity’ defined such that equality holds at a given temperature. In our control experiment, with  $\text{OLR} \approx 240 \text{ Wm}^{-2}$  and  $T \approx 280\text{K}$ , we find  $\epsilon \approx 0.6 \text{ (Wm}^{-2}\text{K}^{-1}\text{)}$ . Given a change in global-mean temperature, one can then relate the clear-sky adjustments to the first-order Taylor expansion about the control state:

$$\text{Adj}_{\text{clear}} = -\frac{d\text{OLR}}{dT} \cdot \delta T \approx -4\epsilon\sigma T^3 \cdot \delta T \quad (2)$$

This scaling is found to reproduce most of the variance in clear-sky rapid adjustments in our experiments (Supplementary Fig. 2).

### Aquaplanet simulations

We run our ICON aquaplanet simulations for 10 years, with the first year discarded as spin-up and analysis conducted on time-averages of the final 9 years. The SST is prescribed in each experiment, with the zonal-mean SST taken as the ‘control’ distribution from Neale and Hoskins (2000)<sup>64</sup>, in addition to a wavenumber-2 SST dipole which spans one half-hemisphere and takes the form,

$$\delta\text{SST} = 3\cos(2\lambda)\cos\left(\frac{\pi}{2}\left[\frac{\phi}{\phi_0}\right]\right) \quad \text{for } -\frac{\pi}{4} < \lambda < \frac{3\pi}{4}.$$

Here  $\lambda$  is the longitude,  $\phi$  is the latitude and  $\phi_0 = \frac{\pi}{6} = 30^\circ$  is the latitudinal width of the perturbation. The amplitude of the dipole is thus  $\pm 3\text{K}$ . The AA perturbations are prescribed at regular longitude intervals spanning between the peaks of the SST dipole (Supplementary Fig. 5) and the aerosol properties are identical to those used in the main experiments.

### Stream-function calculation

To calculate the zonal-mass stream-function for tropical overturning, we first use the *windspharm* library<sup>65</sup> to calculate the divergent component of the zonal wind,  $u_{\text{div}}$ , using a Helmholtz decomposition<sup>66</sup> and then calculate the zonal-mass stream-function at each pressure,  $p$ , and latitude,  $\phi$ , using:

$$\psi(\phi, p) = \frac{2\pi R_e}{g} \int_{1000\text{hPa}}^p u_{\text{div}}(p', \phi) dp'.$$

Here  $R_e$  is the earth’s radius. To plot longitude-pressure cross-sections, we then average  $\psi$  between  $\pm 20^\circ$  of the equator using area-weighting.

0 **Indonesian plume experiments**

1 We conduct experiments with the realistic climatology of Indonesian biomass-burning from Stevens et al., (2017), which has a simple  
2 seasonal cycle peaking in the dry season (Supplementary Fig. 7) and a prescribed single-scattering albedo of 0.87. We then run a  
3 series of five, 10-year experiments, with the AOD in each experiment scaled by an extra factor of 2 compared to the climatology. The  
4 vertical profile of the aerosol is the same in each experiment and only the magnitude is varied. The ‘Climatology\_x16’ experiment has  
5 a seasonal cycle of AOD which compares favourably with the 2015/2016 AERONET observations and the results of Kiely et al.,  
6 (2019). For more details see Stevens et al., (2017).

7  
8 **Acknowledgements:** A.W. acknowledges funding from the Natural Environment Research Council, Oxford DTP, Award  
9 NE/S007474/1. P.S. and G.D. were supported by the European Research Council (ERC) project constRaining the EffeCts of Aerosols  
0 on Precipitation (RECAP) under the European Union’s Horizon 2020 research and innovation programme with grant agreement no.  
1 724602. P.S. additionally acknowledges support P.S. additionally acknowledges funding from the FORCeS and NextGEMs project  
2 under the European Union’s Horizon 2020 research program with grant agreements 821205 and 101003470, respectively. D.W.P.  
3 acknowledges funding from NERC project NE/S005390/1 (ACRUISE) as well as from the European Union’s Horizon 2020 research  
4 and innovation programme iMIRACLI under Marie Skłodowska-Curie grant agreement No 860100. G.D. also acknowledges funding  
5 from the Israeli Science Foundation Grant 1419/21. A.W. thanks Tim Woollings, Beth Dingley, Tim Hempel and Laura Kiely for helpful  
6 discussions.

7  
8 **Author contributions:** A.W. conducted the simulations, performed the analysis and wrote the initial manuscript draft. All authors  
9 contributed to the design of the study, interpretation of the results and to the improvement of the manuscript.

0  
1 **Competing Interests statement:** The authors declare no competing interests.

7 **References:**

- 8 1. Naik, V. et al. Short-lived climate forcers. in *Climate Change 2021: The Physical Science Basis.*  
9 Contribution of Working Group I to the Sixth Assessment Report of the Intergovernmental Panel on  
0 Climate Change (eds. Masson-Delmotte, V. et al.) (Cambridge University Press, 2021).
- 1 2. Samset, B. H., Lund, M. T., Bollasina, M., Myhre, G. & Wilcox, L. Emerging Asian aerosol patterns. *Nat.*  
2 *Geosci.* **12**, 582–584 (2019).
- 3 3. Lund, M. T., Myhre, G. & Samset, B. H. Anthropogenic aerosol forcing under the Shared Socioeconomic  
4 Pathways. *Atmospheric Chem. Phys.* **19**, 13827–13839 (2019).
- 5 4. Allen, R. J., Sherwood, S. C., Norris, J. R. & Zender, C. S. Recent Northern Hemisphere tropical expansion  
6 primarily driven by black carbon and tropospheric ozone. *Nature* **485**, 350–354 (2012).
- 7 5. Chemke, R. & Dagan, G. The Effects of the Spatial Distribution of Direct Anthropogenic Aerosols  
8 Radiative Forcing on Atmospheric Circulation. *J. Clim.* **31**, 7129–7145 (2018).
- 9 6. Deser, C. et al. Isolating the Evolving Contributions of Anthropogenic Aerosols and Greenhouse Gases: A  
0 New CESM1 Large Ensemble Community Resource. *J. Clim.* **33**, 7835–7858 (2020).
- 1 7. Voigt, A. et al. Fast and slow shifts of the zonal-mean intertropical convergence zone in response to an  
2 idealized anthropogenic aerosol. *J. Adv. Model. Earth Syst.* **9**, 870–892 (2017).
- 3 8. Chung, E.-S. & Soden, B. J. Hemispheric climate shifts driven by anthropogenic aerosol–cloud interactions.  
4 *Nat. Geosci.* **10**, 566–571 (2017).
- 5 9. Fiedler, S. & Putrasahan, D. How Does the North Atlantic SST Pattern Respond to Anthropogenic Aerosols  
6 in the 1970s and 2000s? *Geophys. Res. Lett.* **48**, e2020GL092142 (2021).
- 7 10. Dagan, G., Stier, P. & Watson-Parris, D. Aerosol Forcing Masks and Delays the Formation of the North  
8 Atlantic Warming Hole by Three Decades. *Geophys. Res. Lett.* **47**, e2020GL090778 (2020).
- 9 11. Shindell, D. T. Inhomogeneous forcing and transient climate sensitivity. *Nat. Clim. Change* **4**, 274–277  
0 (2014).
- 1 12. Samset, B. H. How cleaner air changes the climate. *Science* **360**, 148–150 (2018).

- 2 13. Hoesly, R. M. et al. Historical (1750–2014) anthropogenic emissions of reactive gases and aerosols from the  
3 Community Emissions Data System (CEDS). *Geosci. Model Dev.* **11**, 369–408 (2018).
- 4 14. Smith, C. J. et al. Effective radiative forcing and adjustments in CMIP6 models. *Atmospheric Chem. Phys.*  
5 **20**, 9591–9618 (2020).
- 6 15. Smith, C. J. et al. Understanding Rapid Adjustments to Diverse Forcing Agents. *Geophys. Res. Lett.* **45**,  
7 12,023–12,031 (2018).
- 8 16. Stevens, B. Rethinking the Lower Bound on Aerosol Radiative Forcing. *J. Clim.* **28**, 4794–4819 (2015).
- 9 17. Nordhaus, W. Estimates of the Social Cost of Carbon: Concepts and Results from the DICE-2013R Model  
0 and Alternative Approaches. *J. Assoc. Environ. Resour. Econ.* **1**, 273–312 (2014).
- 1 18. Arias, P. A. et al. Technical summary. in *Climate Change 2021: The Physical Science Basis. Contribution*  
2 *of Working Group I to the Sixth Assessment Report of the Intergovernmental Panel on Climate Change*  
3 (eds. Masson-Delmotte, V. et al.) (Cambridge University Press, 2021).
- 4 19. Brown, H. et al. Biomass burning aerosols in most climate models are too absorbing. *Nat. Commun.* **12**, 277  
5 (2021).
- 6 20. Bony, S. et al. Clouds, circulation and climate sensitivity. *Nat. Geosci.* **8**, 261–268 (2015).
- 7 21. Dagan, G., Stier, P. & Watson-Parris, D. Contrasting Response of Precipitation to Aerosol Perturbation in  
8 the Tropics and Extratropics Explained by Energy Budget Considerations. *Geophys. Res. Lett.* **46**, 7828–  
9 7837 (2019).
- 0 22. Dagan, G., Stier, P. & Watson-Parris, D. An Energetic View on the Geographical Dependence of the Fast  
1 Aerosol Radiative Effects on Precipitation. *J. Geophys. Res. Atmospheres* **126**, e2020JD033045 (2021).
- 2 23. Gill, A. E. Some simple solutions for heat-induced tropical circulation. *Q. J. R. Meteorol. Soc.* **106**, 447–  
3 462 (1980).
- 4 24. Persad, G. G., Ming, Y. & Ramaswamy, V. Tropical Tropospheric-Only Responses to Absorbing Aerosols.  
5 *J. Clim.* **25**, 2471–2480 (2012).
- 6 25. Roeckner, E. et al. Impact of carbonaceous aerosol emissions on regional climate change. *Clim. Dyn.* **27**,  
7 553–571 (2006).

- 8 26. Myhre, G. et al. PDRMIP: A Precipitation Driver and Response Model Intercomparison Project—Protocol  
9 and Preliminary Results. *Bull. Am. Meteorol. Soc.* **98**, 1185–1198 (2017).
- 0 27. Stjern, C. W. et al. Rapid Adjustments Cause Weak Surface Temperature Response to Increased Black  
1 Carbon Concentrations. *J. Geophys. Res. Atmospheres* **122**, 11,462–11,481 (2017).
- 2 28. Shindell, D. & Faluvegi, G. Climate response to regional radiative forcing during the twentieth century. *Nat.*  
3 *Geosci.* **2**, 294–300 (2009).
- 4 29. de F. Forster, P. M., Blackburn, M., Glover, R. & Shine, K. P. An examination of climate sensitivity for  
5 idealised climate change experiments in an intermediate general circulation model. *Clim. Dyn.* **16**, 833–849  
6 (2000).
- 7 30. Shindell, D. T., Voulgarakis, A., Faluvegi, G. & Milly, G. Precipitation response to regional radiative  
8 forcing. *Atmospheric Chem. Phys.* **12**, 6969–6982 (2012).
- 9 31. Persad, G. G. & Caldeira, K. Divergent global-scale temperature effects from identical aerosols emitted in  
0 different regions. *Nat. Commun.* **9**, 3289 (2018).
- 1 32. Sand, M., Berntsen, T. K., Ekman, A. M. L., Hansson, H.-C. & Lewinschal, A. Surface temperature  
2 response to regional black carbon emissions: do location and magnitude matter? *Atmospheric Chem. Phys.*  
3 **20**, 3079–3089 (2020).
- 4 33. Kasoar, M., Shawki, D. & Voulgarakis, A. Similar spatial patterns of global climate response to aerosols  
5 from different regions. *Npj Clim. Atmospheric Sci.* **1**, 1–8 (2018).
- 6 34. Field, R. D., van der Werf, G. R. & Shen, S. S. P. Human amplification of drought-induced biomass burning  
7 in Indonesia since 1960. *Nat. Geosci.* **2**, 185–188 (2009).
- 8 35. Field, R. D. et al. Indonesian fire activity and smoke pollution in 2015 show persistent nonlinear sensitivity  
9 to El Niño-induced drought. *Proc. Natl. Acad. Sci.* **113**, 9204–9209 (2016).
- 0 36. Kiely, L. et al. New estimate of particulate emissions from Indonesian peat fires in 2015. *Atmospheric*  
1 *Chem. Phys.* **19**, 11105–11121 (2019).
- 2 37. Kasoar, M. et al. Regional and global temperature response to anthropogenic SO<sub>2</sub> emissions from China in  
3 three climate models. *Atmospheric Chem. Phys.* **16**, 9785–9804 (2016).

- 4 38. Haywood, J. M. & Shine, K. P. The effect of anthropogenic sulfate and soot aerosol on the clear sky  
5 planetary radiation budget. *Geophys. Res. Lett.* **22**, 603–606 (1995).
- 6 39. Hoskins, B. J. & Karoly, D. J. The Steady Linear Response of a Spherical Atmosphere to Thermal and  
7 Orographic Forcing. *J. Atmospheric Sci.* **38**, 1179–1196 (1981).
- 8 40. Sobel, A. H., Nilsson, J. & Polvani, L. M. The Weak Temperature Gradient Approximation and Balanced  
9 Tropical Moisture Waves. *J. Atmospheric Sci.* **58**, 3650–3665 (2001).
- 0 41. Bjerknes, J. ATMOSPHERIC TELECONNECTIONS FROM THE EQUATORIAL PACIFIC. *Mon.*  
1 *Weather Rev.* **97**, 163–172 (1969).
- 2 42. Chen, J., Dai, A., Zhang, Y. & Rasmussen, K. L. Changes in Convective Available Potential Energy and  
3 Convective Inhibition under Global Warming. *J. Clim.* **33**, 2025–2050 (2020).
- 4 43. Anshari, G., Peter Kershaw, A. & van der Kaars, S. A Late Pleistocene and Holocene pollen and charcoal  
5 record from peat swamp forest, Lake Sentarum Wildlife Reserve, West Kalimantan, Indonesia.  
6 *Palaeogeogr. Palaeoclimatol. Palaeoecol.* **171**, 213–228 (2001).
- 7 44. Johnson, B. T., Haywood, J. M. & Hawcroft, M. K. Are Changes in Atmospheric Circulation Important for  
8 Black Carbon Aerosol Impacts on Clouds, Precipitation, and Radiation? *J. Geophys. Res. Atmospheres* **124**,  
9 7930–7950 (2019).
- 0 45. Large Aerosol Radiative Forcing due to the 1997 Indonesian Forest Fire - Podgorny - 2003 - Geophysical  
1 Research Letters - Wiley Online Library.  
2 <https://agupubs.onlinelibrary.wiley.com/doi/10.1029/2002GL015979>.
- 3 46. Gaveau, D. L. A. et al. Major atmospheric emissions from peat fires in Southeast Asia during non-drought  
4 years: evidence from the 2013 Sumatran fires. *Sci. Rep.* **4**, 6112 (2014).
- 5 47. Forster, P. et al. The Earth’s energy budget, climate feedbacks, and climate sensitivity. in *Climate Change*  
6 *2021: The Physical Science Basis. Contribution of Working Group I to the Sixth Assessment Report of the*  
7 *Intergovernmental Panel on Climate Change* (eds. Masson-Delmotte, V. et al.) (Cambridge University  
8 Press, 2021).

- 9 48. Stevens, B. et al. The Added Value of Large-eddy and Storm-resolving Models for Simulating Clouds and  
0 Precipitation. *J. Meteorol. Soc. Jpn. Ser II* **98**, 395–435 (2020).
- 1 49. Koch, D. & Del Genio, A. D. Black carbon semi-direct effects on cloud cover: review and synthesis.  
2 *Atmospheric Chem. Phys.* **10**, 7685–7696 (2010).
- 3 50. Stevens, B. et al. Atmospheric component of the MPI-M Earth System Model: ECHAM6. *J. Adv. Model.*  
4 *Earth Syst.* **5**, 146–172 (2013).
- 5 51. Tiedtke, M. A Comprehensive Mass Flux Scheme for Cumulus Parameterization in Large-Scale Models.  
6 *Mon. Weather Rev.* **117**, 1779–1800 (1989).
- 7 52. Nordeng, T.-E. Extended versions of the convective parametrization scheme at ECMWF and their impact  
8 on the mean and transient activity of the model in the tropics. 41 (1994) doi:10.21957/e34xwhysw.
- 9 53. Sundqvist, H., Berge, E. & Kristjánsson, J. Condensation and Cloud Parameterization Studies with a  
0 Mesoscale Numerical Weather Prediction Model. *Mon. Weather Rev. - MON WEATHER REV* **117**,  
1 (1989).
- 2 54. Lohmann, U. & Roeckner, E. Design and performance of a new cloud microphysics scheme developed for  
3 the ECHAM general circulation model. *Clim. Dyn.* **12**, 557–572 (1996).
- 4 55. Pincus, R. & Stevens, B. Paths to accuracy for radiation parameterizations in atmospheric models. *J. Adv.*  
5 *Model. Earth Syst.* **5**, 225–233 (2013).
- 6 56. Mlawer, E. J., Taubman, S. J., Brown, P. D., Iacono, M. J. & Clough, S. A. Radiative transfer for  
7 inhomogeneous atmospheres: RRTM, a validated correlated-k model for the longwave. *J. Geophys. Res.*  
8 *Atmospheres* **102**, 16663–16682 (1997).
- 9 57. Leuenberger, D., Koller, M., Fuhrer, O. & Schär, C. A Generalization of the SLEVE Vertical Coordinate.  
0 *Mon. Weather Rev.* **138**, 3683–3689 (2010).
- 1 58. Forster, P. M. et al. Recommendations for diagnosing effective radiative forcing from climate models for  
2 CMIP6. *J. Geophys. Res. Atmospheres* **121**, 12,460–12,475 (2016).
- 3 59. Gates, W. L. AN AMS CONTINUING SERIES: GLOBAL CHANGE--AMIP: The Atmospheric Model  
4 Intercomparison Project. *Bull. Am. Meteorol. Soc.* **73**, 1962–1970 (1992).

- 5 60. Stevens, B. et al. MACv2-SP: a parameterization of anthropogenic aerosol optical properties and an  
6 associated Twomey effect for use in CMIP6. *Geosci. Model Dev.* **10**, 433–452 (2017).
- 7 61. Ban-Weiss, G. A., Cao, L., Bala, G. & Caldeira, K. Dependence of climate forcing and response on the  
8 altitude of black carbon aerosols. *Clim. Dyn.* **38**, 897–911 (2012).
- 9 62. Kim, H., Kang, S. M., Hwang, Y.-T. & Yang, Y.-M. Sensitivity of the Climate Response to the Altitude of  
0 Black Carbon in the Northern Subtropics in an Aquaplanet GCM. *J. Clim.* **28**, 6351–6359 (2015).
- 1 63. Kinne, S. et al. MAC-v1: A new global aerosol climatology for climate studies. *J. Adv. Model. Earth Syst.*  
2 **5**, 704–740 (2013).
- 3 64. Neale, R. B. & Hoskins, B. J. A standard test for AGCMs including their physical parametrizations: I: the  
4 proposal. *Atmospheric Sci. Lett.* **1**, 101–107 (2000).
- 5 65. Dawson, A. Windspharm: A High-Level Library for Global Wind Field Computations Using Spherical  
6 Harmonics. *J. Open Res. Softw.* **4**, e31 (2016).
- 7 66. Local partitioning of the overturning circulation in the tropics and the connection to the Hadley and Walker  
8 circulations - Schwendike - 2014 - *Journal of Geophysical Research: Atmospheres* - Wiley Online Library.  
9 <https://agupubs.onlinelibrary.wiley.com/doi/10.1002/2013JD020742>.
- 0  
1

## Supplementary Files

This is a list of supplementary files associated with this preprint. Click to download.

- [williamsetal2021supplement.docx](#)